Statistically assessing vertical change on a sandy beach from permanent laser scanning time series

Kuschnerus, Mieke; Lindenbergh, Roderik; Vos, Sander; Hanssen, Ramon

DOI
10.1016/j.ophoto.2023.100055

Publication date
2023

Document Version
Final published version

Published in
ISPRS Open Journal of Photogrammetry and Remote Sensing

ISPRS Open Journal of Photogrammetry and Remote Sensing 11 (2024) 100055

Contents lists available at ScienceDirect

ISPRS Open Journal of Photogrammetry and Remote Sensing

journal homepage: www.journals.elsevier.com/isprs-open-journal-of-photogrammetry-and-remote-sensing

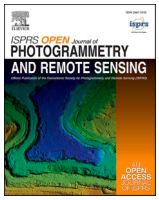

Statistically assessing vertical change on a sandy beach from permanent laser scanning time series

Mieke Kuschnerus [a,*], Roderik Lindenbergh [a], Sander Vos [b], Ramon Hanssen [a]

[a] Department of Geoscience and Remote Sensing, Delft University of Technology, Stevinweg 1, Delft, 2628CN, the Netherlands
[b] Department of Hydraulic Engineering, Delft University of Technology, Stevinweg 1, Delft, 2628CN, the Netherlands

ARTICLE INFO

MSC:
0000
1111

Keywords:
Laser scanning
LIDAR
Multi-temporal 3D point cloud analysis
Permanent laser scanning
Error budget
Multiple hypothesis testing
Minimal detectable bias

ABSTRACT

In the view of climate change, understanding and managing effects on coastal areas and adjacent cities is essential. Permanent Laser Scanning (PLS) is a successful technique to not only observe notably sandy coasts incidentally or once every year, but (nearly) continuously over extended periods of time. The collected point cloud observations form a 4D point cloud data set representing the evolution of the coast provide the opportunity to assess change processes at high level of detail. For an exemplary location in Noordwijk, The Netherlands, three years of hourly point clouds were acquired on a 1 km long section of a typical Dutch urban sandy beach. Often, the so-called level of detection is used to assess point cloud differences from two epochs. To explicitly incorporate the temporal dimension of the height estimates from the point cloud data set, we revisit statistical testing theory. We apply multiple hypothesis testing on elevation time series in order to identify different coastal processes, like aeolian sand transport or bulldozer works. We then estimate the minimal detectable bias for different alternative hypotheses, to quantify the minimal elevation change that can be estimated from the PLS observations over a certain period of time. Additionally, we analyse potential error sources and influences on the elevation estimations and provide orders of magnitudes and possible ways to deal with them. Finally we conclude that elevation time series from a long term PLS data set are a suitable input to identify aeolian sand transport with the help of multiple hypothesis testing. In our example case, slopes of 0.032 m/day and sudden changes of 0.031 m can be identified with statistical power of 80% and with 95% significance in 24-h time series on the upper beach. In the intertidal area the presented method allows to classify daily elevation time series over one month according to the dominating model (sudden change or linear trend) in either eroding or accreting behaviour.

1. Introduction

In the view of climate change and the intensification of extreme weather events it is essential that coastal areas are monitored regularly with high accuracy. Permanent laser scanning (PLS) is an emerging measurement technique used to monitor natural areas including glaciers (Kellerer-Pirklbauer et al., 2005), rockfall (Abellán et al., 2010) and coasts (Vos et al., 2017), as well as structures such as buildings, pipelines or mines (Mukupa et al., 2017; Vezočnik et al., 2009). PLS consists of a terrestrial laser scanner scanning frequently from a fixed position. With large amounts of point cloud data becoming increasingly manageable and improved instrumental set-ups, frequent terrestrial laser scanning (TLS), airborne laser scanning (ALS) as well as PLS are becoming well-established. PLS has the potential of detecting small scale changes in height or small deformations. The detectable changes reach centimetre levels (Vos et al., 2022; Anders et al., 2019; Schröder and Nowacki, 2021) and time scales of several days up to years are covered in different research projects (Voordendag et al., 2021; Schröder et al., 2022). However, at increased spatial and temporal resolution, environmental influences on the measurement system have a more pronounced effect on their performance (Kuschnerus et al., 2021b) and conventional methods for the determination of estimation quality, as developed for example for height estimations from ALS or TLS observations, do not always suffice.

A short analysis of error sources for height estimates from coastal PLS is presented by Vos et al. (2020) and Kuschnerus et al. (2021b), who find that the strongest influence on the uncertainty in height estimates in a permanent coastal set-up during extreme weather conditions comes from precipitation and strong winds, which can both lead to data loss. Several methods are being developed to analyse geo-morphologically

* Corresponding author.
E-mail address: M.Kuschnerus@tudelft.nl (M. Kuschnerus).

https://doi.org/10.1016/j.ophoto.2023.100055
Received 11 May 2023; Received in revised form 22 November 2023; Accepted 7 December 2023
Available online 27 December 2023

relevant processes in PLS data sets (see Anders et al. (2021); Kuschnerus et al. (2021a); Campos et al. (2021)) without specifically considering quality of height or displacement estimates or minimal detectable changes in elevation or displacement. The *level of detection* as an indication of statistically significant surface change was developed for comparison between point clouds of two epochs by Brasington et al. (2000) and Lane et al. (2003). It is used to determine if differences between two point clouds in any direction are statistically significant for a fixed significance level (generally chosen as 95 %). The level of detection is used in combination with Kalman-filtering to detect significant height changes in 4D data sets by Winiwarter et al. (2023) and for the comparison of differences between two epochs of rough surfaces with the M3C2 algorithm (Lague et al., 2013). Methods that specifically consider multi-temporal point cloud comparison are still being developed and improved. Therefore the following research questions are posed to lead the research for this study:

- What is the minimal change in height on a sandy beach that can be estimated with a given confidence with our permanent laser scanning set-up?
- How do environmental conditions contribute to the uncertainty of height estimates from permanent laser scanning for the identification of change processes?
- Which change processes on a sandy beach can be observed with permanent laser scanning and at which temporal and spatial scales?

To answer these questions, we first introduce the properties of our specific PLS data set, followed by the processing steps leading to time series of digital elevation models (DEMs). Then we present the estimation of errors per grid cell of a DEM generated from each point cloud and the level of detection of height differences between scans. Further we adopt the multiple hypotheses testing methodology by Chang and Hanssen (2016) for PLS data and use the model definitions for the estimation of the *minimal detectable bias* in height estimation. The results cover geometric properties of the example data set, influences of environmental effects on the uncertainty of height estimation and a comparison of the concept of the level of detection with the minimal detectable bias. Finally, we consider the detection of two geo-morphologic processes, aeolian sand transport and sudden changes caused by anthropogenic activities, and demonstrate the challenges of the presented method in the intertidal area.

2. Related work

Error sources in terrestrial laser scanning are summarised by Soudarissanane et al. (2011). They emphasise the relevance of scanning geometry as influencing factor on height estimation quality and divide error sources into the following categories: scanner mechanism, atmospheric conditions and environment, object properties and scanning geometry. A review of commonly used performance estimation and error sources was presented by Muralikrishnan (2021) with a focus on standardising the comparison of the quality of different instruments under test conditions.

Typically, accuracy of height estimations in digital elevation models (DEM) from laser scanning is assessed with the help of real-time kinematic positioning (RTK) GNSS measurements, as for example presented by Hladik and Alber (2012) and Hodgson and Bresnahan (2004). Bitenc et al. (2011) use a theoretical error model in combination with overlapping LiDAR point clouds from mobile mapping to generate DEMs with corresponding error estimation. Rigorous theory on error models has been developed among others by Glennie (2007) and by Lichti (2007). These models require the acquisition of extensive self-calibration data sets under controlled laboratory conditions, which are not available in the case of many practical applications.

More recently Kerekes and Schwieger (2020) developed an improved elementary error model (EEM) for height estimates from laser scanning with consideration of atmospheric effects on the measurements and therefore estimation accuracy. Winiwarter et al. (2021) use error model theory to improve point cloud distance calculation based on a modified M3C2 algorithm as presented by Lague et al. (2013), which was developed mainly for irregular rocky surfaces, as applied for example by Zoumpekas et al. (2021) and for the comparison of two epochs. For more regular and flat surfaces Wheaton et al. (2010) and Milan et al. (2007) extend the theory of the level of detection to quantify uncertainty in DEMs of elevation differences (DoD) on river beds incorporating various error sources and error propagation. These techniques can be applied to a multi-epoch PLS data set as well, but the specific opportunities and challenges that arise from dealing with (nearly) continuous elevation time series have not been considered. A recent study by Voordendag et al. (2023) discusses the five main influences on uncertainty of height estimates from PLS measurements of a glacier in the Alps. Their method is based on Soudarissanane (2016) and derives the uncertainty in height estimation per DEM grid cell from single point measurements combined with registration errors. Williams et al. (2018) consider a modified version of the M3C2 algorithm to detect volume change of rock falls. Williams et al. (2018) conclude that higher temporal resolution can improve detection of instantaneous events, but simultaneously increases the accumulated estimation error for small-magnitude long-term processes.

Hypothesis testing is a well-established statistical technique. It was introduced by Baarda (1968) for geodetic applications, and presented among others by Teunissen (2006). Lindenbergh (2010) use hypothesis testing to group and classify elevation times series from six consecutive point clouds. A rigorous approach on how to apply multiple hypotheses tests (MHT) on estimated kinematic InSAR time series was presented by Chang and Hanssen (2016). They define a model data base to provide multiple alternative hypothesis and then use statistical testing, to identify the most likely kinematic model for each time series. The advantages and challenges of this method for the use on a large 4D data set from laser scanning of a very dynamic area, such as the coast, have not been discussed. We propose a simple way to use MHT for two basic models to identify geo-morphologic processes on different time scales. The term *Minimal detectable bias* for multiple hypothesis testing was first introduced by Baarda (1968) and is discussed in detail by Imparato et al. (2019). The minimal detectable bias (MDB) gives a measure of a minimum change in the estimated quantity of a time series that is needed in order to be identified with statistical significance.

For the comparison of two DEMs and calculating the statistical significance of the elevation difference per grid cell it is commonly assumed that both height estimates in the respective grid cell are normally distributed. Adding the systematic registration error σ_{reg} and applying statistical testing using Gaussian statistics (based on Borradaile and Borradaile (2003)) results in the level of detection (LOD) at the 95% confidence interval as presented for example by Lague et al. (2013). For the M3C2 algorithm a normal vector is determined from a neighbourhood around the considered point. This step can be skipped in the case of comparing two DEMs, since all height estimates of the DEMs are measured in z-direction. Thus, the necessity of the use of M3C2 or its advanced versions (Winiwarter et al., 2021) is absent and the only remaining step is the estimation of the level of detection. The level of detection, LoD, between two grid cells in two DEMs with estimated variances σ_i^2 and number of points per grid cell n_i, $i \in \{1, 2\}$ and registration error σ_{reg}, as defined by Lague et al. (2013) is given by

$$\mathrm{LoD} = \pm 1.96 \cdot \left(\sqrt{\frac{\sigma_1^2}{n_1} + \frac{\sigma_2^2}{n_2}} + \sigma_{reg} \right). \tag{1}$$

The estimated variances contain the terrain roughness as well as measurement precision. The level of detection is therefore a statistical confidence interval at a chosen significance level, here 95% for the difference between two independent surface elevations, with normally

distributed measurement errors. This approach has also been applied to time series, where each height estimate per epoch was compared with the respective level of detection to a height estimate at the reference epoch, usually the first measurement (Winiwarter et al., 2023).

3. Data acquisition and properties

3.1. Instrument specifications and settings

The point clouds are collected with a Riegl VZ-2000 laser scanner, which is permanently mounted on the balcony of Grand Hotel Huis ter Duin in Noordwijk, The Netherlands. The laser scanner is mounted on a metal frame at 55.757 m height above NAP (elevation above the Amsterdam Ordnance Datum) that is fixed to the balcony to maximise stability. The scanner is covered with a protective housing (see Fig. 1) to shield it from rain, wind and dust.

The specifications and settings of the laser scanner are summarised in Table 1. Each point cloud is generated by running a scan of nearly 180° covering a part of the beach of just under 1 km every hour with angular spacing of 0.03°.

The system is set up with the same instrument and instrumental settings as a previous experiment at a different location, see Vos et al. (2022).

3.2. Data availability

The laser scanner generates one 3D point cloud per scan, made up of x, y, z-coordinates which are derived by the Riegl proprietary software out of observed range, horizontal and vertical angle data. The laser scanner also observes the intensity of the backscattered signal, per point. The internal inclination sensor records inclination values during each scan, with a frequency of 1 Hz (not matching the scanning frequency).

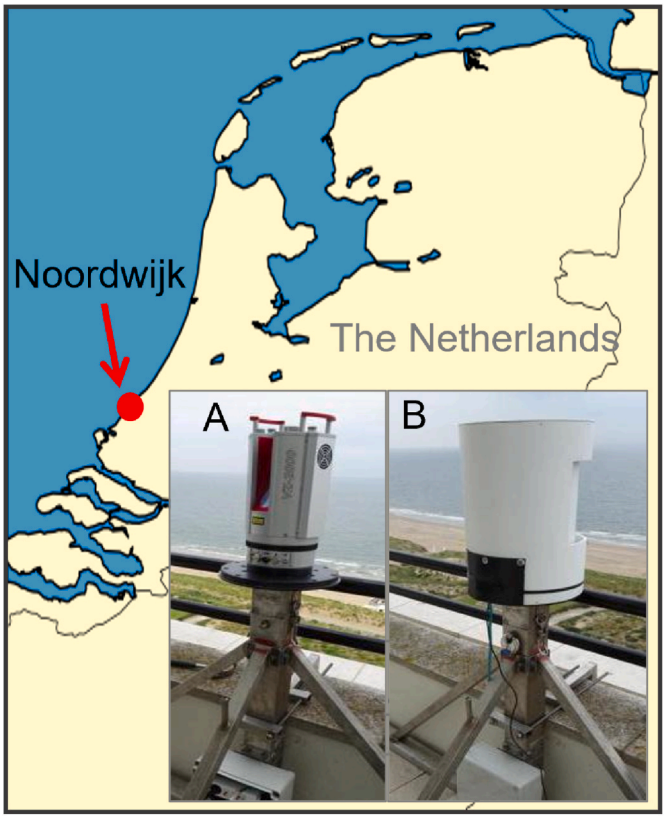

Fig. 1. Location of the study site on the Dutch coast in Noordwijk, The Netherlands and picture of the laser scanner mounted on a hotel balcony without (A) and with (B) protective cover.

Table 1
Specifications of Riegl VZ-2000 laser scanner according to documentation.

range accuracy (at 150 m range) [m]	0.008
angular spacing [deg]	0.003
beam divergence [mrad]	0.3
wavelength [nm]	1550
inclination sensor	
measurement accuracy [deg]	0.008

These inclination angles are used for correction of tilts in the scanner (see section 4.1) and have a measurement accuracy of 0.008°.

The scanner operates 24 h a day for the duration of three years. The numbers of available point clouds are visualised in Fig. 2. A few gaps appear in the data collection. Some of them result from bad weather conditions, but most are due to technical failure and organisational problems. In May 2020 a decline in the data quality (i.e. increased presence of randomly located noise points) was observed and the scanner was finally switched off and sent for maintenance for a 34-day period at the end of June 2020 until end of July 2020. In December 2021 the scanner stopped working due to an unknown issue. Because of the holiday season it was not noticed until 18 days later in January 2022, when the scanner was restarted. The entire point cloud data set is published via 4TU Research Data (Vos et al., 2023).

Additionally we collect data from a nearby weather station to separate environmental influences from other factors affecting the height estimation quality. We consider temperature, average wind speed per hour and precipitation as main influences on our height estimations. At the same time temperature, atmospheric pressure and humidity are provided to the instrument for internal range correction. These values are provided by meteoserver.nl and read from nearby local weather stations of the Royal Netherlands Meteorological Institute (KNMI) (Koninklijk Nederlands Meteorologisch Instituut, 2022) and updated hourly, to match the scanning frequency. For comparison and evaluation of results we use wind and temperature data from the KNMI weather station in Hoek van Holland, on the coast at about 38 km distance from the laser scanner and to compare with visibility data we use measurements from a weather station in Schiphol, at about 25 km distance, but more inland.

3.3. Study area and test areas

The observed area includes a sandy beach and dunes, covered with vegetation and is about 1 km long and 250 m wide. The beach is strongly influenced by the tides and varies in width between 80 m and 140 m under normal weather conditions. The area includes a helicopter landing platform (at 135 m range), which is used as a stable reference surface and a beach cafe at the dune foot on the sandy beach (at about 172 m range), which causes a large shadow area on the sandy beach, as shown in Fig. 3.

For this study we focus on the sandy beach and disregard the dunes, parts of the hotel captured by the scanner and all points representing

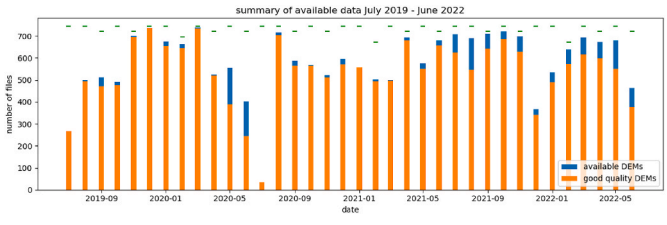

Fig. 2. Available point clouds per month over the entire three-year period. The green dashes show the maximum number of files that would be possible per month. Two large gaps in the data collection are visible in June/July 2020 (maintenance) and in December 2021/January 2022, where the scanner stopped operating unnoticed during the holiday season.

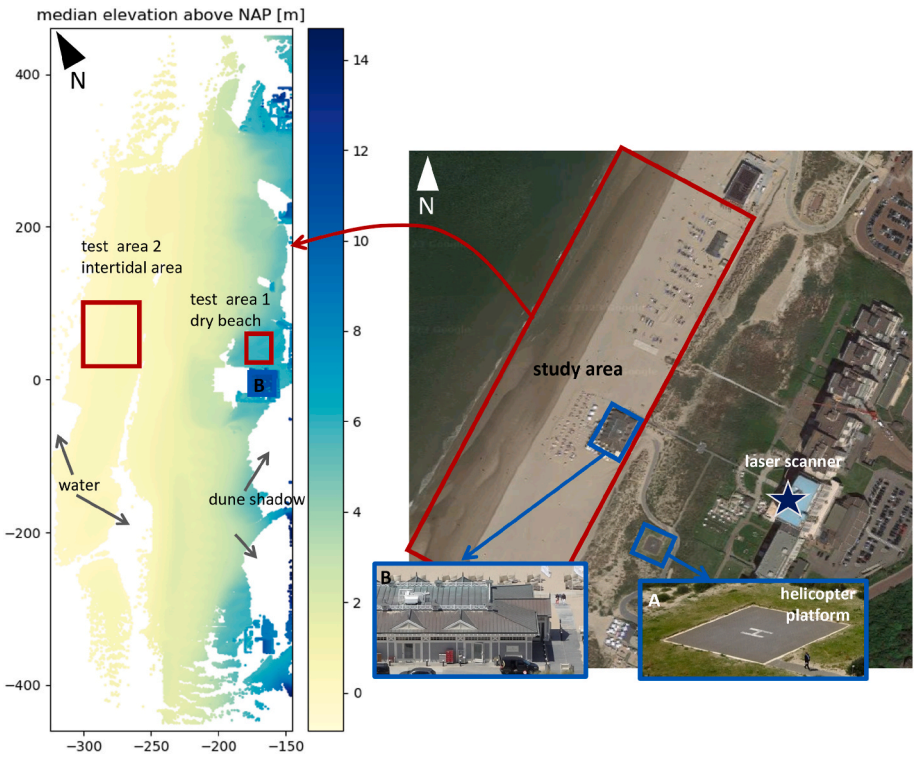

Fig. 3. Top view of DEM of the area of interest at low tide on 14-04-2020 (left panel) with marked test areas on the dry beach and in the intertidal area. White areas in the DEM represent shadows of the dunes, buildings or flooded parts in the intertidal area, where the scanner is not recording any points. The x- and y-axis represent across-shore and along-shore distance in meters. Right panel: Overview of study site, located on the beach in Noordwijk (Google maps) with helicopter platform (A) and beach cafe (B) which serve as stable reference surfaces. The location of the laser scanner is marked with a star.

vegetation or other non ground objects (people, rubbish bins, etc.). A few reference surfaces (see Fig. 3) from within the dune area are considered as well for the estimation of the registration error. The height above NAP of the reference surfaces has been confirmed with RTK-GNSS measurements and double checked with height estimates from the AHN (Actueel Hoogtebestand Nederland) measurement campaigns (GeoTiles.nl, 2021) using ALS. The range of the sandy beach varies within the point cloud between 150 and 500 m. On the beach we selected two exemplary test areas, as marked in Fig. 3. Test area 1, at about 180 m range is representative of the dry part of the beach, where the tide does not reach under normal weather conditions. Because of the location right next to the beach cafe, it is subject to frequent bulldozer works and human activities. Test area 2, at about 290 m range, appears only a few times a day in the point clouds, as it is regularly submerged during high tide. Point spacing varies between 1 and 40 points per m^2 with non-overlapping, ellipse shaped footprints (short diameter between 0.04 and 0.08 m and long diameter between 0.11 and 0.8 m) with sizes ranging from 0.015 m^2 to 0.27 m^2. We assume that the height estimation per point represents the estimated height at the centre location of the footprint. The incidence angle is rather unfavourable due to a surface slope of about 1° (on average) towards the sea and the position of the laser scanner. It ranges between 72 and 80° on the sandy part of the beach. A schematic of the side view of the set up and distances to the beach is shown in Fig. 4 together with an illustration of the number of points and foot print size within a square meter at 145 m range.

4. Method

4.1. Pre-processing workflow

The workflow is shown as a schematic in Fig. 5 and explained in the following paragraphs.

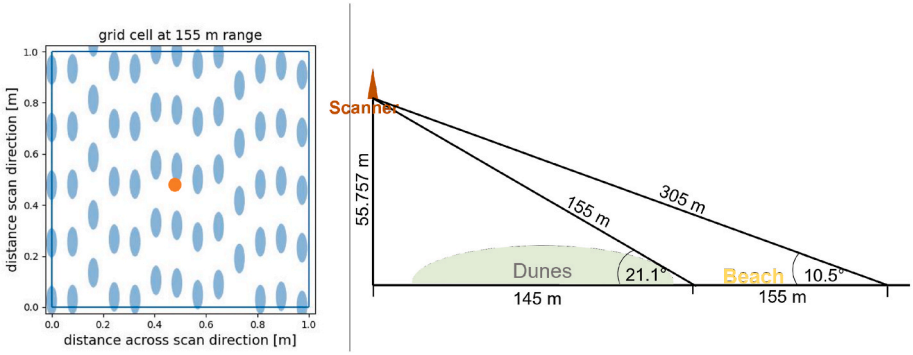

Fig. 4. Left: Illustration of estimated footprint size and distribution within a square meter on the closest part of the beach (at about 155 m range). All height estimates within a square meter are averaged to estimate the height at the grid cell centre (marked in orange) to generate a DEM (see Section 4.1). Right: Schematic side view of the instrument set up and range to the beach at different horizontal distances.

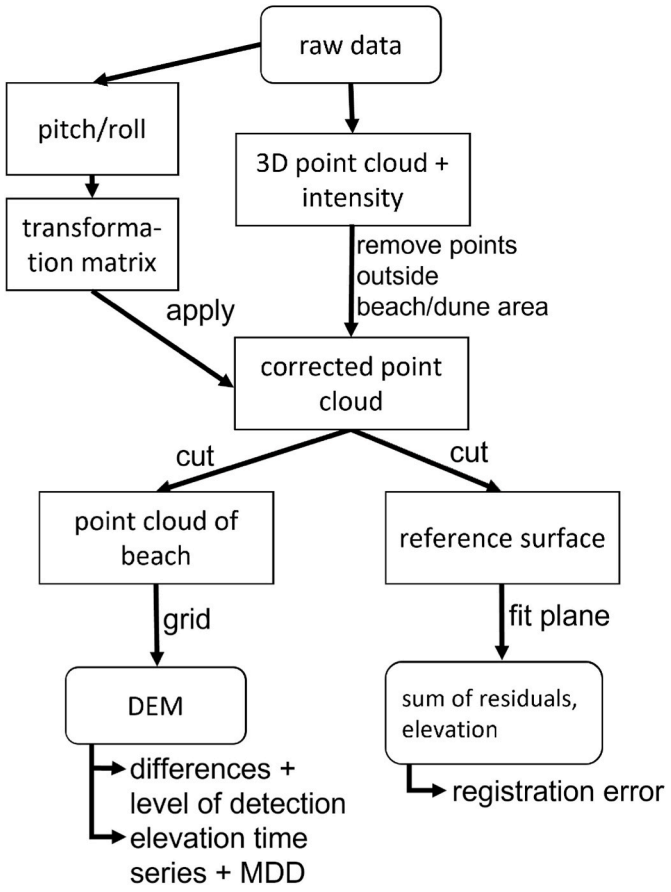

Fig. 5. Flow chart of the pre-processing steps.

4.1.1. Preparation of data

Each 3D point cloud is in a local coordinate system with the location of the laser scanner as its origin. We determined the height of the laser scanner when it was mounted with the help of a GNSS receiver. This constant elevation of 55.757 m above NAP is added to the z-coordinate, to process actual height above sea level instead of negative elevation with respect to the scanner's location.

In a first step, all points representing the hotel are removed from each point cloud. This leads to a reduction in size of each point cloud from about 5 Mio points to about 3.5 Mio relevant points.

4.1.2. Correction of scanner tilt

In a next step the 1 Hz inclination measurements from the laser scanner are averaged for each scan and the mean pitch and roll inclination are estimated. These values are then used to calculate a rotation matrix **R**:

$$\mathbf{R} = \begin{pmatrix} \cos(\varphi) & 0 & \sin(\varphi) \\ \sin(\varphi)\sin(\theta) & \cos(\theta) & -\cos(\varphi)\sin(\theta) \\ -\sin(\varphi)\cos(\theta) & \sin(\theta) & \cos(\varphi)\cos(\theta) \end{pmatrix} \tag{2}$$

with φ the pitch angle and θ the roll angle. The rotation matrix **R** is calculated for each point cloud separately and applied only, if the standard deviations of the pitch and roll values during the entire acquisition of the respective point cloud are below a threshold. This is to ensure that point clouds acquired during a heavy storm are not corrected with a rotation based on erroneous inclination values. In these cases a mean pitch and roll value based on the other scans in that month is used for correction. A constant general tilt of the point cloud is removed in this way, as well as the main part of deviations of the laser scanner's position due to temperature changes (heat expansion of building and supporting structure) or strong winds (see Section 5.1).

4.1.3. DEM generation

For the following analysis of the systematic error affecting each point cloud and for a quality check, the reference surfaces are cut out using their x- and y-coordinates. We assume that the reference surfaces are flat with constant elevation and no tilt in x- or y-direction. Plane fitting provides the mean elevation of the respective reference surface as well as the squared sum of residuals between all points and the fitted plane. Both are used for a quality check: If the mean elevation of the plane deviates more than 0.1 m from the (GNSS verified) expected elevation or the squared sum of residuals is above 0.1 m^2, the respective point cloud is marked as 'bad quality' and not considered for further analysis. In Fig. 2 these files are indicated as available (blue) but not included as 'good quality DEM' (orange).

For further analysis of elevation changes on the beach and in the test areas, all other parts of the point cloud are removed and subsequently a DEM is generated from the remaining points, covering only the sandy part of the beach. The DEM has a 1m $\times$ 1m grid cell size and the mean elevation of all points is used as grid cell elevation estimate located at the centre of the grid cell (Fig. 4, left). For each grid cell the accumulation of the estimated elevations over time provides the elevation time series at that location.

4.2. Error influences

For further analysis we investigate the random error affecting each grid cell of the DEM, σ_g, and the systematic error affecting the entire point cloud, ε_{pc}. To summarise and quantify the most relevant error influences we estimate the order of magnitude for each of them following Soudarissanane (2016) and Voordendag et al. (2023), and distinguish the main influences: geometry, registration, atmosphere, instrument and surface properties.

4.2.1. Geometry and registration

We assume that the measurement geometry does not change between scans, except for slight movement of the scanner, due to strong wind and movement of the entire hotel building due to concrete expansion. After correction of scanner tilt (see Section 4.1), the largest part of the geometric error is removed. A small error, due to the limited measurement accuracy of the inclination sensor will remain and we do not have the means to quantify any changes in yaw-angle. Since the start and stop angle of each scan are settings that are kept constant, we do not take into account any errors due to inaccuracies in yaw direction. The effect of concrete expansion can be estimated from temperature observations using the expansion coefficient (see for example Marshall (1972)) and is estimated to be below 1 cm. However, direct correlation with our measurements and correction of this error prove to be difficult. We do not take into account variations of incidence angle and footprint size, which both vary within the scene as well as over time with changes in the surface topography (see Table 2).

No additional registration step is applied. Therefore, small registration errors are still present when comparing subsequent point clouds. We observe the registration error on elevation measurements by analysing the height of a fitted plane through the stable reference surfaces.

Table 2
Summary of data properties. The summary considers all hourly scans between 11 July 2019 and 21 June 2022.

area covered	250 000m^2
days scanned	954
interruptions (> 24h)	21
number of points per point cloud	$8.5 \cdot 10^6$
number of points (beach)	800 000
range (beach)	145 – 500 m
point density (beach)	1 – 40 pt/m^2
footprint size (beach)	0.015 – 0.27 m^2
incidence angle (beach)	70 – 90 deg

The small variations observed here (in the order of 1.5 cm) are the result of slight displacements of the scanner, scanner tilt and expansion of the building where the scanner is mounted on and potentially disturbances of the atmosphere. We cannot separate these effects and therefore summarise them in one error term ε_{pc} including all error sources affecting the entire point cloud systematically.

4.2.2. Atmosphere

Atmospheric effects were found to influence the height estimates as reported by Kuschnerus et al. (2021b). Deviations in range and therefore in elevation can be caused by temperature gradients in the air and therefore differences in refraction index between the scanner location and right above the beach. The order of magnitude can be estimated empirically from elevation time series of the reference surfaces. Assuming the atmosphere does not vary within the area of interest, the atmospheric effects are part of the systematic error ε_{pc}. Low visibility due to fog prevents measurements all together and leads to exclusion of the respective point cloud. For more explanation on the effect of atmospheric changes on height estimates from PLS see Voordendag et al. (2023).

4.2.3. Instrument

Instrument errors can result from environmental effects: temperature fluctuations could influence the instrument. It is not known what the exact temperature under the protective cover and inside the instrument is at the time of data acquisition. Therefore, the temperature from a nearby weather station is possibly not representative for the temperature inside the laser scanner. Additionally, the laser scanner showed some erroneous behaviour in spring and early summer 2020. Point clouds acquired at this time contained more and more additional random points above and below the actual measured surface. These points were for a large part filtered out. The erroneous measurements could be part of the grid cell uncertainty σ_g. However, when filtering for mean elevation and summed residuals on the reference surfaces as explained in Section 3.2, the point clouds heavily affected by the malfunction, were excluded. Calibration of the instrument and long-term drifts in calibration parameters could potentially influence our measurements as well. However, two calibration reports at the beginning of the scan and after maintenance in summer 2020 did not show any significant changes.

4.2.4. Surface properties

Surface properties in our test areas are relatively consistent, since we are interested in observing the sandy beach. They vary, however in soil moisture and surface roughness. Soil moisture content has an effect on reflectivity (Di Biase et al., 2021; Jin et al., 2021) and potentially affects range measurements. Surface roughness was further analysed by Di Biase et al. (2022) where different grid cell size and variogramms of surface roughness were considered. All error terms affecting the grid cell are summarised as σ_g (equation (3)).

4.3. Error estimation

We estimate the elevation in z-direction per grid cell as the mean elevation over all points within the grid cell. This corresponds to the simplified plane equation, where the estimated elevation $\hat{z}$ is just the mean of all observed values z_i from the vector of observations $\underline{\mathbf{z}}$ as in Bitenc et al. (2011): $\hat{z} = \text{mean}(\underline{\mathbf{z}})$. The surface roughness and measurement uncertainty are then incorporated in the standard deviation of all points in the grid cell, which corresponds to the root mean square error (RSME) σ_g. We define σ_g by

$$\sigma_g = \sqrt{\frac{\underline{\mathbf{e}}_s^T \underline{\mathbf{e}}_s}{n_p - 1}}, \tag{3}$$

for the spatial residual vector $\underline{\mathbf{e}}_s$ of all elevation values in the grid cell and number of points $n_p - 1$, to ensure an unbiased estimation.

The systematic errors are dominated by the registration error plus temperature and atmospheric effects as explained above. It is estimated from the mean elevation of the reference surfaces and does not vary significantly with range, because the rotation part is largely corrected and the remaining translations affect the entire point cloud independent of location. We assume that the observed standard deviation of the elevation of the fitted plane provides the systematic error $\varepsilon_{pc} = 1.5$ cm for the entire point cloud.

4.4. Hypothesis testing for time series

To allow classification of time series according to likely deformation models, we apply multiple hypothesis testing based on the approach by Chang and Hanssen (2016). More details and background can be found in the work of Teunissen (2006) and some examples in Tiberius et al. (2021). MHT allows to test for the null-hypothesis (no change) and several alternative hypotheses.

With the definitions as above, we consider the entire time series of one grid cell location, with elevation vector $\underline{\mathbf{y}} = (\hat{z}_1, \hat{z}_2 \ldots, \hat{z}_m)$ over time $\underline{\mathbf{t}}$ of length m and corresponding vectors of standard deviations $\underline{\sigma}_g$ and number of points per grid cell $\underline{\mathbf{n}}_p$.

We assume that the elevation vector $\underline{\mathbf{y}}$ can be estimated with the model $\underline{\mathbf{y}} = \mathbf{A} \cdot \underline{\mathbf{x}} + \underline{\mathbf{e}}_t$ for an unknown parameter vector $\underline{\mathbf{x}}$ of dimension n. The temporal residual vector $\hat{\underline{\mathbf{e}}}_t = \underline{\mathbf{y}} - \mathbf{A} \cdot \hat{\underline{\mathbf{x}}}$, is the estimated temporal residual vector not related to the spatial residuals in Section 4.3. We assume that the single elevation measurements are normally distributed as described above, and therefore the residual vector $\hat{\underline{\mathbf{e}}}_t$ is normally distributed with zero mean (see for example Tiberius et al. (2021) for more details).

Now we define the null-hypothesis H_0 and one alternative hypothesis H_1 following Chang and Hanssen (2016):

$$H_0 : \mathrm{E}(\underline{\mathbf{y}}) = A_0 \cdot \underline{\mathbf{x}} \tag{4}$$

$$D_y = Q_{yy} = \mathrm{diag}(\underline{\sigma}) \tag{5}$$

$$H_1 : \mathrm{E}(\underline{\mathbf{y}}) = A_0 \cdot \underline{\mathbf{x}} + C_1 \underline{\mathbf{b}}_1 \tag{6}$$

$$D_y = Q_{yy} \tag{7}$$

where $\mathbf{A}_0 \in \mathbb{R}^{m \times n}$ is the design matrix, i.e. representing the model of the null-hypothesis, $E(\cdot)$ the expectation operator and $\mathbf{D}_y$ is the dispersion which equals the covariance $\mathbf{Q}_{yy} \in \mathbb{R}^{m \times m}$ of the elevation vector $\underline{\mathbf{y}}$. For the alternative hypothesis H_1, the model is extended by a specification matrix $\mathbf{C}_1$ with $\underline{\mathbf{b}}_1$ the additional vector of unknown parameters. To either sustain or reject the null-hypothesis, considering the normal distribution of the residual vector $\hat{\underline{\mathbf{e}}}_t$, we use the χ^2-distribution, $\chi^2(q, \lambda)$, with non-centrality parameter λ and number of additional parameters of the alternative hypotheses q. For the null-hypothesis, the model is simply the mean elevation over the entire time series. In this case the model matrix $\mathbf{A}_0$ reduces to an m-dimensional vector, $n = 1$, yielding null-hypothesis H_0 and test value T_0

$$H_0 : \mathbf{A}_0 = \begin{pmatrix} 1 \\ 1 \\ \vdots \\ 1 \end{pmatrix}, \quad x = x_0 \tag{8}$$

$$T_0 \sim \chi^2(1, 0). \tag{9}$$

As first alternative hypothesis we use a step function defined to test for sudden changes at time $\hat{t}$, with elevation $x_0 = \text{mean}(y_1 \ldots y_{\hat{t}-1})$ for $t < \hat{t}$ and $x_1 = \text{mean}(y_{\hat{t}} \ldots y_m)$ for $t \geq \hat{t}$, and dimensions $n = 2$ and additional parameter dimensions $q = 1$, yielding alternative hypothesis $H_{1,\hat{t}}$ and test value $T_{1,\hat{t}}$:

$$H_{1,\hat{t}} : \mathbf{A}_{1,\hat{t}} = \begin{pmatrix} 1 & 0 \\ \vdots & \vdots \\ 1 & 0 \\ 0 & 1 \\ \vdots & \vdots \\ 0 & 1 \end{pmatrix}, \quad x = \begin{pmatrix} x_0 \\ x_1 \end{pmatrix} \tag{10}$$

$$T_{1,\hat{t}} \sim \chi^2(1, \lambda). \tag{11}$$

With $\mathbf{C}_{1,\hat{t}} = (0, \ldots, 0, 1, \ldots, 1)^T$ and $b_{1,\hat{t}} = x_1 - x_0$ this is equivalent to our previous definition of the alternative hypothesis:

$$H_{1,\hat{t}} : \quad \mathrm{E}(\underline{\mathbf{y}}) = \mathbf{A}_0 \cdot \underline{\mathbf{x}} + \mathbf{C}_{1,\hat{t}} b_{1,\hat{t}}. \tag{12}$$

The determination of $\hat{t}$ in practice is explained in more detail in Section 4.6.

And as second alternative hypothesis H_2 we use a linear trend and calculate test value T_2:

$$H_2 : \mathbf{A}_2 = \begin{pmatrix} 1 & t_1 \\ \vdots & \vdots \\ 1 & t_m \end{pmatrix}, \quad x = \begin{pmatrix} a_0 \\ a_1 \end{pmatrix} \tag{13}$$

$$T_2 \sim \chi^2(1, \lambda) \tag{14}$$

where a_0 is the intercept and a_1 the slope of the linear model and therefore $\mathbf{A}_2 \in \mathbb{R}^{m \times 2}$, $n = 2$ and $q = 1$. This is consistent with equation (6) when defining:

$$\mathbf{C}_2 = (t_1, \cdots, t_m)^T, \quad b_2 = a_1. \tag{15}$$

The covariance matrix is defined by the RMSE per grid cell (σ_g as defined in Section 4.3). We assume that there is no correlation between subsequent measurements and therefore obtain the diagonal matrix

$$\mathbf{Q}_{yy} = \mathrm{diag}(\sigma_{g1}^2, \ldots, \sigma_{gm}^2) = \underline{\sigma^2} \cdot \mathbf{I}_m. \tag{16}$$

Following Tiberius et al. (2021) and Chang and Hanssen (2016) the test value $T_j, j \in \{0, \ldots, m+1\}$ for time series of length m for all alternative hypotheses, is then calculated as

$$T_j = \underline{\hat{\mathbf{e}}}_{j,t} \, \mathbf{Q}_{yy}^{-1} \, \underline{\hat{\mathbf{e}}}_{j,t} = \sum_{i=1}^{m} \frac{(y_i - \hat{y}_j)^2}{\sigma_i^2}, \tag{17}$$

with residual vector $\underline{\hat{\mathbf{e}}}_{j,t}$ for modelled time series $\underline{\hat{\mathbf{y}}}_j = \mathbf{A}_j \cdot \hat{x}$. The test value is then compared to the critical value k_α, for significance level α following the respective χ^2-distribution, with non-centrality parameter λ.

We test for every grid cell, if for a time series over a fixed amount of time (for example 24 h) the null-hypothesis is not rejected. If it is rejected, we test in a next step, which of the alternative hypothesis is most likely i.e. has smallest value for T_j below the critical value. If T_j is above the critical value for all alternative hypotheses, no adequate model can be found. In this way sudden changes, as well as gradual, linear processes can be identified with a pre-defined level of confidence α. This method is suitable to be extended for periodic/seasonal changes or any other typical behaviour that one would expect on a sandy beach.

4.5. Test quality

The type I error describes the rejection of the null hypothesis, while it is true. The size of the type I error is the probability of this happening and is defined by significance level α. The size of the type II error is given by the probability of a missed detection of change (in height in our case), β. Its compliment is the detectability power $\gamma = 1 - \beta$, see Fig. 6 for an illustration. The determination of the detectability power γ therefore depends on the calculation of the probability of a missed detection β, which is defined as the integral of the probability density function of the alternative hypothesis over the acceptance region of the null-hypothesis (see Fig. 7).

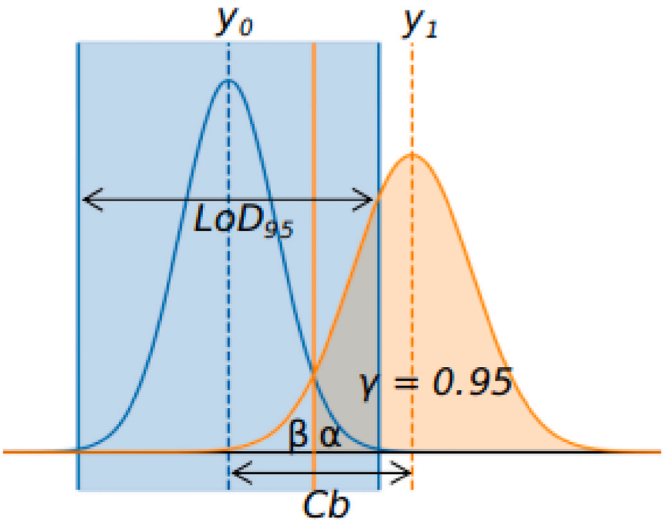

Fig. 6. Comparison of level of detection with detectability power. The parameters α and β are indicated and they both equal 0.05 in this example. It can be seen that the level of detection with significance level 95% does not match the minimal detectable bias with 95% detectability power.

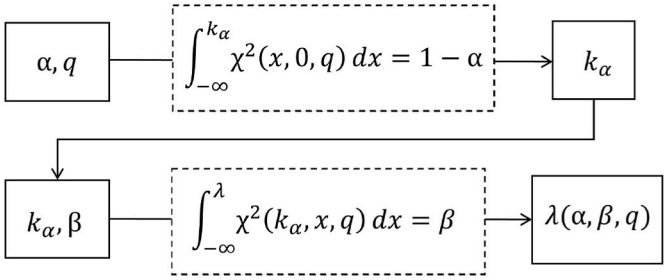

Fig. 7. Schematic of the calculation of the non-centrality parameter $\lambda(\alpha, \beta, q)$. With $\chi^2(x, \lambda, q)$ we denote the probability density function of the non-central χ^2-distribution for (non-)centrality parameter λ and with degrees of freedom q.

For the multiple hypothesis testing, following the core idea of Baarda's B-method, also applied by Chang and Hanssen (2016), the detectability power is fixed, for example at 80% and the significance level α can be defined depending on the number of parameters of the respective hypothesis, as well as the dimension of the time series. Then, the critical value T_j will be evaluated in relation to the significance level and the ratios will be compared instead of the critical values, since the significance level depends on the number of parameters of the alternative hypothesis. Here, we choose two simple models for the alternative hypothesis, which both have two parameters that need to be estimated. Therefore the critical values can be compared directly and the discriminatory power, and consequently the type II error will be the same for all alternative hypothesis with the above definitions.

4.6. Minimal detectable bias

To answer our first research question, we use the concept of the *minimal detectable bias*, as introduced by Baarda (1968), assuming we know which model(s) would best represent possible changes in elevation (alternative hypotheses) in a specific area and time period. In our case, we are looking for the minimal height of a step in a sudden change (step function model) and the minimal slope (height per hour) that we can detect with the specified test set up. Following Baarda and the more recent works by Imparato et al. (2019) and Teunissen (2006), the

minimal detectable bias can be determined by reversing the above procedure to calculate the detectability power γ and therefore fixing the type II error. Instead of calculating the integral of the probability density function of the alternative hypothesis, we fix $\gamma = 0.8$ (i.e. 80 % probability of correct detection), with now known model matrix $\mathbf{C}$ and covariance matrix $\mathbf{Q}_{yy}$. We check the value of the central normal distribution for the selected value of $\beta = 1 - \gamma$, and use it to invert the equations, which leads to the minimal detectable bias.

In a first step towards determining the MDB, we calculate the non-centrality parameter of the χ^2-distribution, $\lambda(\alpha, \beta, q)$ for significance level α and $\beta = 1 - \gamma$, where γ is the detectability power of the test, and number of additional parameters q. In a first step the central χ^2-distribution is used to get the critical value k_α, that is the value where the integral over the central χ^2-distribution with degrees of freedom q reaches the value $1 - \alpha$. Then we loop over all possible non-centrality values λ, to find $\lambda(\alpha, \beta, q)$, where the integral of the non-central χ^2-distribution for k_α as previously found and with degrees of freedom q reaches probability β.

The equation for the minimal detectable bias for our case of known diagonal covariance matrix Q_{yy} reduces to:

$$\mathrm{MDB} = \sqrt{\frac{\lambda(\alpha, \beta, q)}{\mathbf{C}^T \mathbf{Q}_{yy}^{-1} \mathbf{C}}}. \tag{18}$$

For the respective alternative hypotheses defined above that simplifies to:

$$\mathrm{MDB}_{step} = \sqrt{\frac{\lambda(\alpha, \beta, q)}{\sum_{i=i}^{m} \sigma_i^{-2}}}, \tag{19}$$

indicating the minimum value of the step at location $\hat{t}$ for $H_{1,\hat{t}}$ and

$$\mathrm{MDB}_{lin} = \sqrt{\frac{\lambda(\alpha, \beta, q)}{\sum_{i=1}^{m} t^2 / \sigma_i^2}}, \tag{20}$$

indicating the minimum slope value for a linear function for H_2.

As illustration, Fig. 8 shows an example time series with MDB for two different models of alternative hypotheses: the height of a step function for a step after the 10th epoch and the slope of a linear trend starting at the first epoch. The step was assumed at a fixed location at $\hat{t} = 10$, without any further consideration of other alternative hypotheses (i.e. for different values of $\hat{t}$). We consider three different cases: Varying detectability power γ (Fig. 8A), varying significance level α (Fig. 8B) and in Fig. 8C for both γ and α fixed and the same time series with larger uncertainty and lower uncertainty. It can be seen that larger detectability power γ and lower significance level α both lead to larger values of MDB. Additionally, higher standard deviation on the time series lead to larger values of MDB than lower standard deviations.

For comparison with the previously mentioned level of detection, this situation has been drawn for a simple 1-dimensional case in Fig. 6. For the presented definition of the level of detection (see Section 2), the first test parameter to define is the significance level α, which determines the type I error and is mostly chosen at 5%. Here we show the level of detection with 95% confidence interval around the mean value y_0. The mean value for the alternative hypothesis y_1 is shown as the minimal detectable bias when assuming $\gamma = 0.95$ (i.e. 95% probability of correct detection) in order to make them comparable. It can clearly be seen that y_1 is outside the level of detection region and the two terms do not coincide or provide the same insight.

5. Results

5.1. Effects of environmental conditions on estimation quality

The effect of weather conditions on the height estimation quality was analysed in terms of mean elevation, before and after the tilt correction, as well as wind speed. Strong precipitation and fog, which both affect visibility, clearly have degrading effect on height estimations and most scans under these conditions will be excluded and not pass the quality criteria. In our entire data set, we find 156 cases, where point clouds were not available at the same time that fog or low visibility conditions were registered at the KNMI weather station at Schiphol airport. Schiphol is at about 25 km distance from the study site in Noordwijk, so the weather conditions could differ. But it gives an indication, that out of more than 5000 instances, where point clouds are not available, less than 3 % are possibly caused by low visibility.

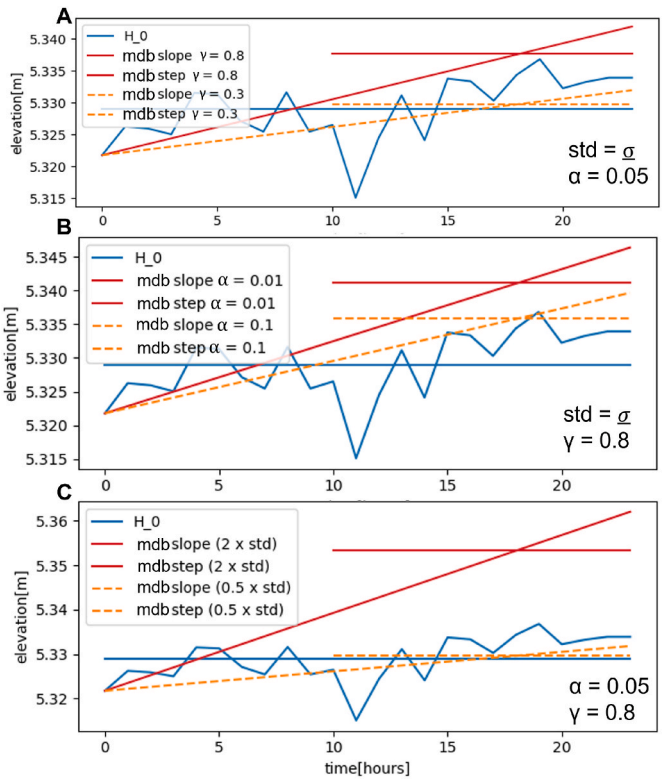

Fig. 8. minimal detectable bias (MDB) for a time series covering 24 h with two different alternative hypotheses: a step function, with a step at the 10th epoch and a linear function with positive slope. A: Both hypotheses are shown for different values of detectability power γ: 0.2 and 0.8. B: Both hypotheses are shown for different values of significance level α: 0.01 and 0.1. C: Both hypotheses are shown for fixed significance level and detectability power (α = 0.05 and $\gamma = 0.8$) with different standard deviations: half standard deviation from the previous cases and doubled standard deviation.

The order of magnitude of the main influences on the uncertainty of the height estimate (z-coordinate) within the point cloud (on each grid cell) and on the entire point cloud are summarised in Table 3. We summarise, which effects are corrected or filtered out (scanner tilt and instrument failure) and how the others contribute to the two error terms σ_g and ε_{pc}. How temperature, wind speed and direct sunshine affects these uncertainty estimates is explained in more detail in the following subsections.

5.1.1. Temperature effects

An example of the effect of temperature is shown for a period of six days in August 2019, with mostly clear skies, no precipitation and relatively low wind speed (average 4.5 m/s) in Fig. 9. An obvious pattern in the mean elevation of the reference surface before correction is visible. The 24-h pattern corresponds to duration of sunshine per hour as well as temperature. Considering the entire six-day period, temperature as well as sunshine show negative correlation with the uncorrected

Table 3
Summary of estimated order of magnitudes for each of the influences on uncertainty affecting the entire point cloud or the grid cell in z-direction.

Influence	Estimated order of magnitude	Explanation
Corrected and removed influences		
Scanner tilt	10 - 20 cm	Estimated from inclination angles and corrected
Instrument	≥10 cm	Errors due to instrument failure, affected point clouds are removed from analysis
Not corrected and considered in error terms ε_{pc} and σ_g		
Concrete expansion	0.7 cm	Estimated from temperature variations, not corrected, included in systematic error ε_{pc}
Registration	}1.5cm	Estimated from elevation of reference surfaces, not corrected, included in systematic error ε_{pc}
Atmosphere/ temperature		
Surface roughness	0.9–7 cm	Estimated per grid cell, considered as random error σ_g
Surface moisture/ footprint size		Not quantified or corrected, included in random error σ_g

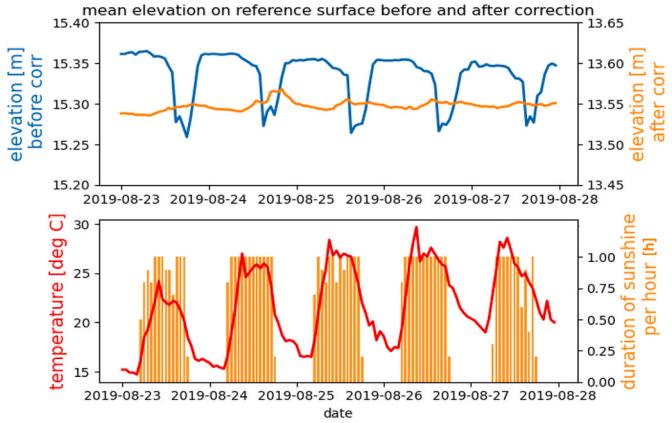

Fig. 9. Time series of mean elevation over the course of six days in August 2019 on the helicopter landing platform before tilt correction (A) and after tilt correction (C) with duration of sunshine per hour (A) and temperature(B).

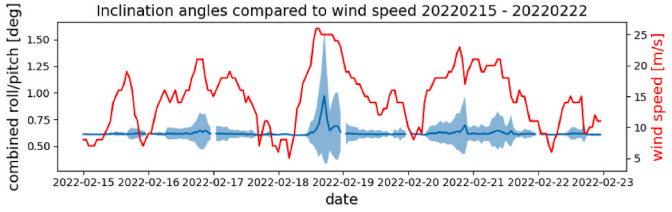

Fig. 10. Combined inclination angles (squared sum of pitch and roll) with standard deviation and wind speed.

mean elevation (-0.32 and -0.26 respectively). After correction, sunshine and mean elevation are not correlated anymore, but temperature and mean elevation now show a positive correlation of 0.28. When looking at the fast Fourier transformation (FFT) of the elevation, a slight 24-h signal can be detected, which is probably the cause of the correlation with temperature. However, as can be seen in Fig. 9, the main part of the 24-h pattern in the elevation can be corrected for (see Fig. 10).

The remaining signal could be attributed to expansion of the concrete of the hotel building. An upward shift of the entire scanning set-up cannot be registered by the instrument's inclination sensors. The rotation correction is therefore not suitable to correct for this type of error. The concrete expansion, on days with highly varying temperatures, is estimated using the concrete expansion coefficient and the height of the building. It can amount to up to 0.7 cm elevation change, within several hours or days (not within the hour). However, we could not correlate the estimated concrete expansion directly with the remaining variation in elevation on the reference surfaces.

5.1.2. *Effects of wind speed*

To show the effect of wind on the height estimation from PLS, we first visualise the combined pitch and roll angle (squared sum) together with wind speed, and show a clear correlation between standard deviation of inclination values and wind speed (0.71) and a lower correlation between mean inclination and wind speed (0.47) for seven stormy days in February 2022, as an example. As was shown by Kuschnerus et al. (2021b), the effect of the higher standard deviation can be visible in the point clouds as a striped pattern on the reference surface. There, it was also shown that during strong winds, the sum of residuals on the reference surface is higher, and most likely related to the high standard deviation in the inclination values. For this example period in February 2022, we did not find a correlation between the sum of residuals on the reference platform and the inclination values or the wind speed.

Further, considering the entire data set, we did not find any correlation between wind speed and the residuals on the reference surface. This shows, that the residuals in general are not that sensitive to wind and that the corrected point clouds are suitable for further analysis with the errors explained above. However, of the cases where there is a point cloud available, but the quality is not good enough, about 34 % occurred during strong winds (8 m/s and higher), which indicates a possible causal relation.

5.2. *Differentiating dynamic processes on the beach*

First, we show the minimal detectable bias for test area 1 on the dry beach and two alternative hypotheses. Then, we perform the multiple hypothesis testing (as introduced in Section 4.4) on both test areas, but for different length of time series and show the resulting partitioning of the areas according to the most likely estimated model.

5.2.1. *Minimal detectable bias*

We show the minimal detectable bias for test area 1 as indicated in Fig. 3: On the dry beach, next to the beach cafe and frequently used by people as well as effected by bulldozer works. We estimate the MDB as explained in Section 4.6 with detectability power $\gamma = 80\%$ and with significance level $\alpha = 95\%$.

As an example to illustrate the MDB on the dry test area we use 24-h time series from 7 of January 2020. The MDB is calculated for a sudden change in form of a step function happening at 17:00h in the afternoon and shown in Fig. 11. We know that bulldozer works started that day and moved a considerable amount of sand between 11:00h and 17:00h depending on location, as reported previously Kuschnerus et al. (2022). The MDB shows, what the minimum change in elevation per grid cell would have to be at that time, in order to be detected as significant. We incorporate the systematic error ε_{pc} in order to derive a realistic estimate. The resulting minimal detectable bias ranges from 1.8 cm (just above the ε_{pc}) up to 32 cm for some outliers, with a median at 3.1 cm. As comparison we show the LoD as defined above, which has a median value of 26.8 cm for the entire area, which is one order of magnitude higher than the MDB with our configuration. The MDB and the average value of the LoD indicated in Fig. 16, are representative of one dot in Fig. 11A and C respectively. The MDB for a linear trend was calculated as well: Only a few grid cells appear to deviate a lot from the median slope of 3.2 cm/day, see Fig. 11B.

5.2.2. *Hypothesis testing*

We applied the multiple hypothesis testing as explained in Section 4.4 on the time series of each grid cell in the previously described test areas, using 24-h time series on 7 January 2020.

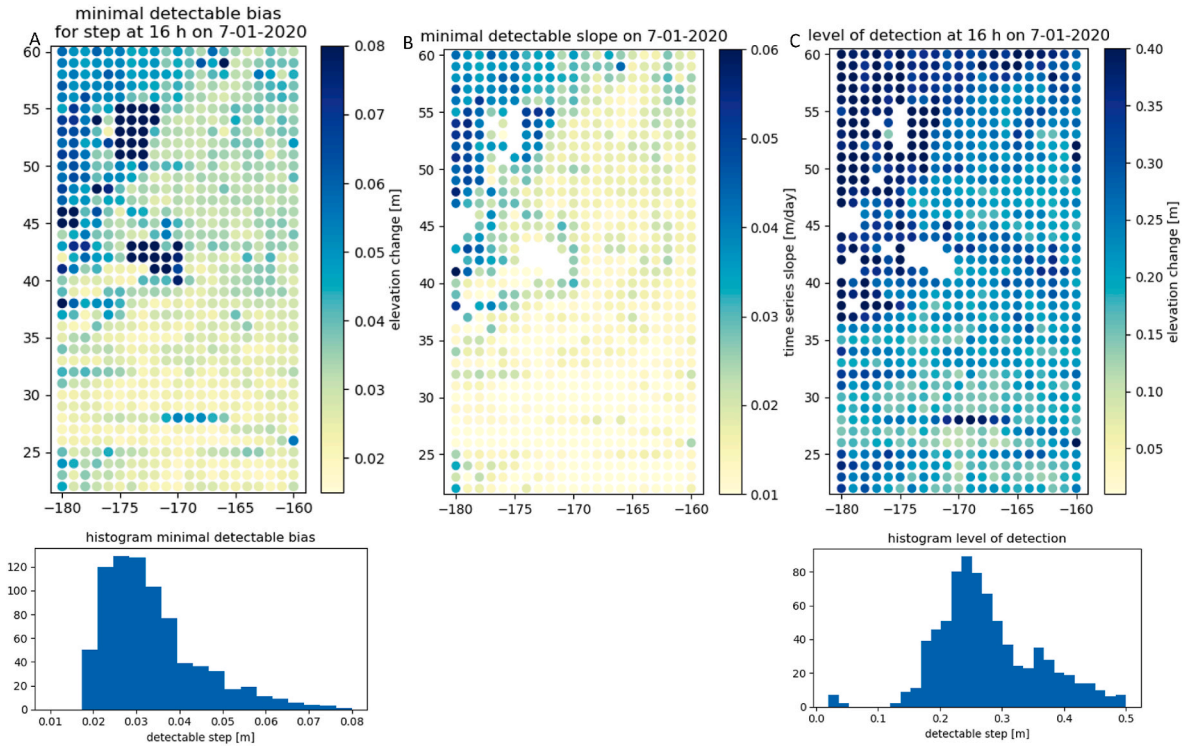

Fig. 11. minimal detectable bias at significance level $\alpha = 0.05$ and with detectability power $\gamma = 0.8$ for a step function with step at 17:00h (A) and a linear trend (in m/day) (B). Results were calculated for each 24-h time series on 7 January 2020. For comparison the level of detection is shown for a significant change at 17:00h (C). To simplify the comparison of the spread of the values for the MDB and LOD the histograms of the respective estimates are shown as well.

Using the above described testing method for the test area on the dry part of the beach we identify sudden changes, most likely caused by bulldozer works, as mentioned before. The changes happen between 16:00 and 17:00 in the afternoon and are identified on a large part of the area (see Fig. 12). Fig. 12 shows some example time series with no significant change and sudden changes.

Similar to results shown in previous works (Kuschnerus et al., 2021a, 2022; Barbero-García et al., 2023), human activities on the beach like bulldozer works that lead to sudden elevation changes can be detected and quantified. Multiple hypothesis testing for 24-h elevation time series with a step function as alternative hypothesis allows to find and identify most bulldozer works taking place on the sandy beach.

To identify longer term and slower processes, we apply the same testing procedure to time series in the same area, covering the entire month of July 2021, with two epochs per day, at noon and at midnight. Again we can classify the testing area into the three classes: no change,

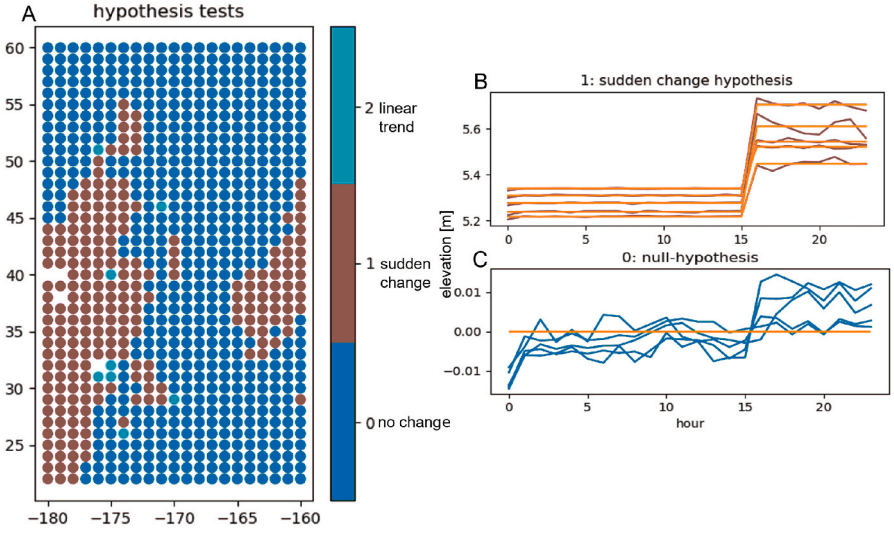

Fig. 12. A: Dry area classified according to hypothesis testing based on time series covering 24 h on 07-01-2020. The x- and y-axis represent across-shore and along-shore distance in meters. B: Example time series with sudden change hypothesis sustained. The changes happened at 16:00h in the afternoon. C: Example time series over 24 h with null-hypothesis not rejected, i.e. no statistically significant change detected. The small step occurring in some time series around 16:00h is not significant enough to be detected.

sudden change and linear trend. Here we find more areas with a linear change. However, for some cases a two-(or more)step model would seem more appropriate, as can be seen in Fig. 13B. The sudden change model does not fit the time series very well, since in a longer term time series, it is more likely that more than one sudden change occurs (see Fig. 13 C).

In Fig. 13B slow erosion processes are identified. The area close to the dune foot shown in panel A of the same figure is eroding with about 0.5 cm per day. A slow, gradual erosion process like this can be caused by aeolian sand transport or possibly by frequent use of beach visitors crossing that area. It is however unique to observe the gradual changes over a long period of time and quantify the erosion at sub-centimetre level.

When considering test area 2 (as indicated in Fig. 3) in the intertidal area of the beach, fully populated daily time series are not available. The area appears in the point clouds only once (or sometimes twice) per day, during low tide. A set of daily time series in September 2020, with one epoch per day, chosen at low tide, where the area of non-empty grid cells in the DEM is largest, was analysed using MHT. Fig. 14 shows some examples of the classified time series (B) and an overview of the entire area coloured with the most likely assumed hypothesis (A). Here we distinguish between erosion (negative) and deposition (positive) versions of the found model time series, to give more insight in the present dynamics.

It becomes apparent that the two models used for the alternative hypotheses are not sufficient to classify all processes affecting the beach. The model library can be extended with other models and additionally the start and stop time of the time series that is classified should be chosen individually per time series in order to fit the available models better. Still a general trend of either eroding or accreting becomes apparent in the overview plot (Fig. 14A) and the more dynamic nature of the intertidal area is clearly visible. The observed effects are most likely the result of tides and waves depositing and eroding sand while the area is flooded every day.

6. Discussion

6.1. Additional effects on estimation quality

Since the laser scanner is pointed to the west, the sun could directly shine into the lens of the scanner in the hours just before sunset. Since we do not have weather data from directly next to the laser scanner for most of the time, there is no way to verify when this situation occurred. We collect all point clouds, acquired a few hours before and up to the time of sunset on that day and check if they pass our quality checks. All point clouds with low quality collected just before or at sunset could potentially be affected by direct sun shine. We filtered out all instances with high wind speeds (above 8 m/s) and precipitation (more than 1 mm/h). There are 10 instances, where around the time of sunset, the quality of the DEM was not good enough (i.e. the residuals on the reference surface were too high, compare threshold defined in section 4.1) during or in the hours before sunset. All of them occurred in the summer months of 2019, outside of the period of malfunction of the laser scanner. The respective point clouds show some noise (i.e., random points in the air), but the cause of this noise could not be determined with certainty. We observed a similar effect in the weeks leading up to the maintenance of the scanner in spring 2020, when the general quality of height estimations declined due to the previously mentioned instrument malfunction. With a ray-tracing method as for example presented by Zhou et al. (2019) the times with direct sunshine into the laser scanner could be determined with more certainty, which would allow more investigation into possible effects on the respective point clouds.

Beach visitors show up as peaks or outliers in the grid cell time series. As shown in Fig. 15, the hourly time series during a scan by students of the TU Delft show peaks whenever a person was present in the respective grid cell. These outliers are not causing the null-hypothesis to be rejected, but a busy period with lots of beach visitors will lead to higher grid cell error σ_g, which has an impact on the hypothesis testing.

A possible solution to this, would be a filter for dynamic objects on the beach applied to each point cloud before generating the DEMs. This would increase processing times significantly and potentially lead to some data loss, but in return it could make the results of MHT more reliable.

6.2. Potential improvements of set-up and processing

For this research we have made several assumptions and simplifications considering the atmospheric conditions and calibration of the instrument. Additionally we did not consider in detail the slope of the beach, footprint size variation, surface roughness, fine registration and correlation of the height estimates.

For a future improved set-up we recommend installing temperature sensors or even entire weather stations next to the scanner and in the observed scene at various locations. The collected temperature measurements would allow for an estimation of the refraction index and other atmospheric influences. To improve atmospheric correction with the additional atmospheric measurements we suggest to consider the

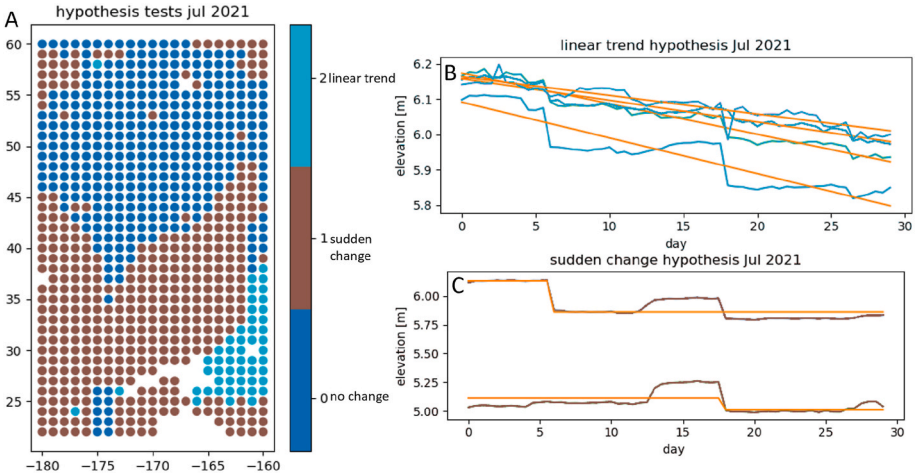

Fig. 13. A: Dry area classified according to hypothesis testing based on time series covering the month of July 2021. The x- and y-axis represent across-shore and along-shore distance in meters. B: Example time series with linear trend (orange). One of the time series (in blue) shows a shape that appears more like two sudden changes. C: Two examples, where the sudden change was found as most likely model (orange), but does not fit the shape of the time series, which shows more than one sudden change.

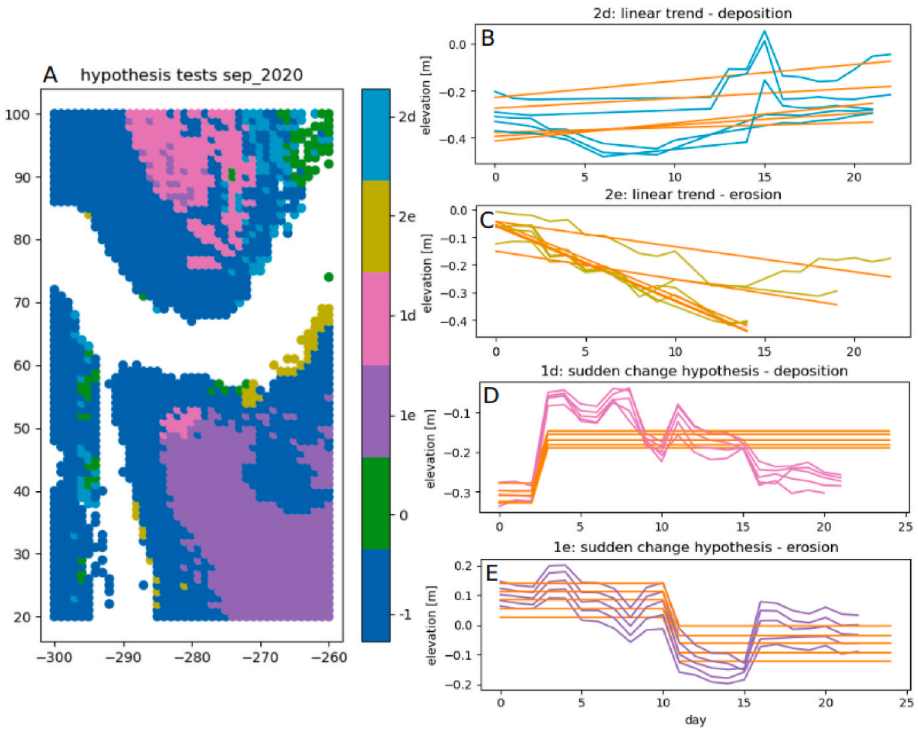

Fig. 14. A: Classification according to most likely assumed hypothesis in the intertidal area, based on daily time series in September 2020. The x- and y-axis represent across-shore and along-shore distance in meters. B-E: Example time series for each of the four assumed models: positive linear trend (deposition, B), negative linear trend (erosion, C), sudden change deposition (D) and sudden change erosion (E). This example illustrates, that the two models used for the alternative hypothesis are not sufficient for many cases and an adaptive length of the time series would improve the results.

approaches of Voordendag et al. (2023) and Czerwonka-Schröder (2023).

Any instrumental error could potentially be further reduced by performing a dedicated calibration in regular time intervals on site, preferably without removing the instrument from its permanent location. This could reduce any drifts in range estimates and yaw alignment and prevent instrument failure and need for maintenance, or at least allow earlier detection leading to reduced data loss. For calibration of terrestrial laser scanners one could consider for example the works of Medic et al. (2019) and Schmitz et al. (2019).

The slope of the beach and with that the incidence angle and their variations through time could be estimated based on point clouds or several neighbouring DEM grid cells. Then, a slope correction could be applied to the individual height estimates. The same holds for the estimation of footprint sizes per grid cell. A mean value for footprint size depending on location and estimated incidence angle could be taken into account for the individual height estimates.

The contribution of the surface roughness to the error per grid cell of up to 7 cm is quite high. There are grid cells on the beach, where a constant elevation is not an appropriate surface model. Examples include the edge of a cliff, deep tire tracks, or channels in the intertidal zone. To take such topography into account one could apply different methods of surface approximation, as for example presented by Kermarrec et al. (2022).

The entire data set could be subject to a fine registration method, aligning all point clouds to a suitable epoch, using for example the iterative closest point (ICP) method. This is a computationally intensive operation, but has been done on a similar data set for example by Vos et al. (2022).

Finally, we did not consider correlation between consecutive height estimates. When dealing with short-term measurements, as in our case the hourly data set, temporal correlation between the individual height estimates is likely. To incorporate a correlation coefficient into the hypothesis testing model, the theory of Baarda can be applied, as for example discussed in Rofatto et al. (2020).

6.3. Comparison to existing methods

Other approaches developed by Anders et al. (2019) and Kuschnerus et al. (2021a) make use of region growing and clustering to extract regions in space and time with similarly behaving time series of elevation (or elevation differences). These methods have the advantage that it does not have to be known previously, what kind of processes are expected, so they can in principle be applied without preknowledge on the occurring changes. Winiwarter et al. (2023) combine Kalman filtering for time series interpolation, level of detection and clustering on extracted features to find dynamic processes that were not previously defined. Also here the authors avoid using prior process knowledge. The level of detection is used here for the comparison of height estimates at each epoch with a reference height. For illustration of the typical use, we consider a 24-h time series on January 7th, 2020 and show all differences to the first epoch, together with the level of detection (blue), see Fig. 16. We use equation (1) with $\varepsilon_{pc} = 0.015$ m as registration error for the calculation of the level of detection. We can therefore derive, at what point the time series deviates from the first epoch with 95% confidence (first type error). We further indicate the MDB for both curves and significance level $\alpha = 95\%$ and detectability power $\gamma = 80\%$.

Non of these methods are specifically taking into account the multi-epoch nature of our data, nor do they efficiently detect processes, affected areas and the nature and/or cause of the process. The here presented method uses previous knowledge on expected processes, in order to determine the temporal sampling, as well as the models for the alternative hypothesis. In this way specific processes can be detected, together with a provided level of confidence. To make this useable for the entire observed area, and more for example periodic processes, the model catalogue can be extended and possibly a combination of the above mentioned clustering methods with MHT could be used to identify relevant areas and/or time intervals in the three-year observation

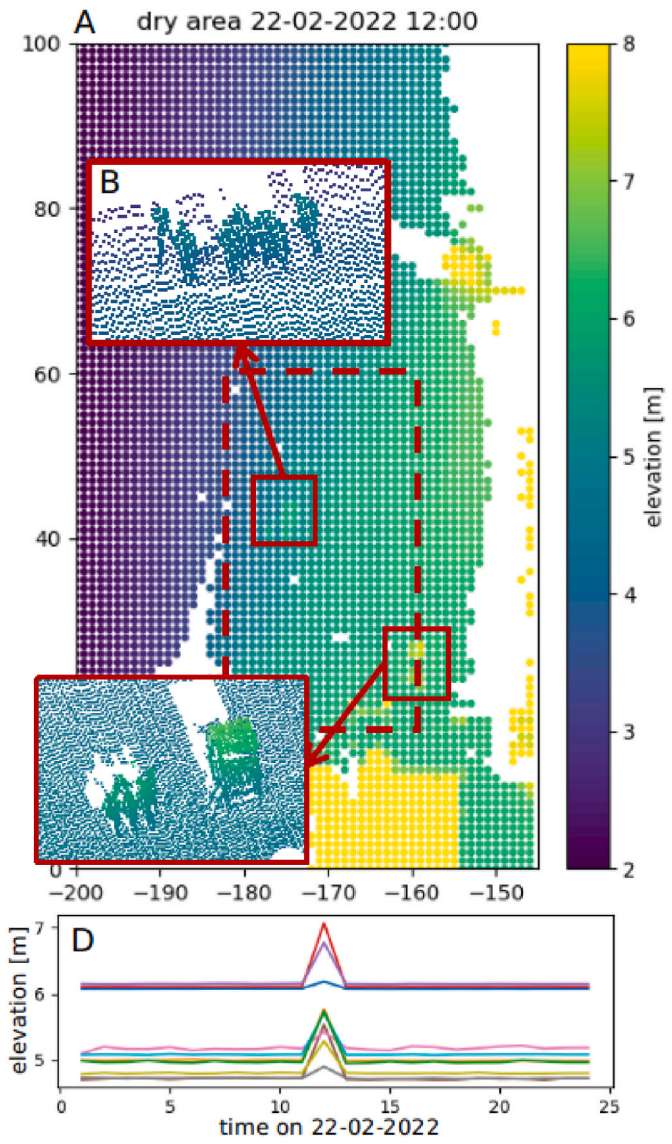

Fig. 15. Effect of beach visitors on the DEM. On 22-02-2022, a group of students visited the study site at the beach and appears in the point cloud at 12:00. The DEM has grid cells of about 80 cm higher than the surroundings at that time (A). The corresponding point clouds showing the people (B,C). The corresponding time series of the entire day show a clear outlier at 12:00 (D).

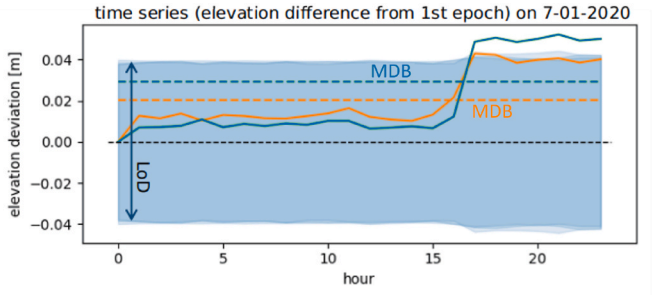

Fig. 16. Example of level of detection for two 24-h time series on 7 January 2020. The time series are shown as difference in elevation from the first epoch. The level of detection is indicated in blue and the MDB for a step function for both time series is shown as a dashed line. The MDB and LoD shown here are different representations of one dot in Fig. 11 A and C, respectively.

period.

We can see in Figs. 12 and 14 that the MHT procedure as applied in this research allows a classification of time series into different processes and therefore also a grouping according to process. The latter has the potential to be used in a similar way or complementary to other methods of clustering time series like (Kuschnerus et al., 2021a) or Winiwarter et al. (2023). The main difference with these methods is the pre-definition of the expected alternative hypotheses. By defining the alternative hypotheses we determine apriori, which processes we are expecting to find. Our search is limited to those processes, but on the other hand provides a level of confidence when detecting them.

For the hypothesis tests the model library can potentially be extended in order to fit more processes present on the beach. More simple functions can easily be added, as for example a periodic elevation change, step functions with several steps or a combination of linear trends and step functions. However, the difficulty in the application will lie in matching the models and the relevant time scales. Considering hourly time series over one day, our simple three model hypothesis testing showed good results in identifying anthropogenic changes, however it did not categorise the intertidal area on monthly time scales well. On larger time scales, other additional models would be required. Therefore, again a priori knowledge on the length and time scale of the time series and the relevant, expected processes is needed in order to identify geomorphological coastal processes in a 4D point cloud data set.

6.4. *Assumptions on uncertainty*

Implicitly we make the assumption that larger residuals per grid cell lead to more uncertainty in the knowledge of the mean elevation at that epoch. This assumption holds in many cases, but is difficult to verify in general. There could be cases, for example in the intertidal area, where surfaces are relatively smooth, but with sharp edges, where this assumption is not true. Another case could be a frozen beach during temperature below zero, where the surface roughness stays frozen over several epochs, thus it does not effect the estimation of the model as we are assuming. However, these cases are not generally true, and we assume the chosen approach provides a realistic estimation of the variance in most cases.

We also tested to use a rolling-window standard deviation based purely on the elevation time series, discarding the spatial component/surface roughness but incorporating the temporal domain into the standard deviation. This did not lead to more realistic assumptions on the standard deviation. The temporal component leads to a lower standard deviation (compared to surface roughness) and is highly sensitive to jumps/sudden changes in the time series. The assumption that a sudden change in elevation made our measurements less likely does not hold in most cases and we therefore conclude that the spatial (roughness-based) standard deviation is a better approximation of the true measurement uncertainty.

7. Conclusion and recommendations

We investigated the main effects on height estimates of a 4D point cloud data set from permanent laser scanning and applied multiple hypothesis testing as well as the minimal detectable bias to time series of height estimates from these observations answering the following questions.

What is the minimal change in height on a sandy beach that can be estimated with a given confidence with our permanent laser scanning set-up? The minimal detectable bias is suitable for the estimation of possible elevation changes found within time series from permanent laser scanning. Making use of the long elevation time series available in the PLS data set, the parameters for the estimation of the minimal detectable bias can easily be tuned to detect small scale changes in sandy beach elevation with a defined detectability power and to identify different models of elevation change. This provides advantages over the

commonly used level of detection, especially the known detectability power and the considering of entire elevation time series rather than just pairs of epochs. In our example case, slopes of 0.032 m/day and sudden changes of 0.031 m were identified with statistical power of 80% and with significance 95% in 24-h time series on the upper beach.

How do environmental conditions contribute to the uncertainty of height estimates from permanent laser scanning for the identification of change processes? The main effects on height estimates from PLS are weather conditions such as strong wind causing the instrument to shake and precipitation and instrument malfunctions. When these are filtered out the remaining effects are dominated by the surface roughness and registration error, which we estimate as below 7 cm and 1.5 cm, respectively. Height deviations caused by temperature changes can reach up to 1 cm within a day and are largely corrected by the application of a rotation matrix based on inclination estimates from the scanner's internal inclination sensor.

Which change processes on a sandy beach can be observed with permanent laser scanning and at which temporal and spatial scales? Multiple hypothesis testing allows for the grouping of areas following similar processes. At the same time we are classifying each time series according to the available alternative hypotheses and therefore gain more insight into the predominant change regime. It is especially suitable to detect and quantify slow longer term erosion and accretion processes, which are most likely caused by aeolian sand transport and difficult to observe using other techniques.

The presented methods appear to be promising in the large scale processing and data mining for change processes within a 4D data set from permanent laser scanning. To be applicable to entire elevation time series of length longer than one month, a method to segment each time series and detect break points would allow to treat each segment separately. We could then apply MHT per segment with appropriate models for the alternative hypothesis.

Further investigation of the error sources on the height estimates and quantification of each effect could potentially improve the quality and reliability of height estimates and therefore lead to the detection of even smaller elevation changes and trends in elevation.

The presented method could potentially be adapted for different applications, such as height estimation on glaciers from permanent laser scanning or identification of height changes in vegetation estimated from laser scanning observations.

Declaration of competing interest

The authors declare that they have no known competing financial interests or personal relationships that could have appeared to influence the work reported in this paper.

Acknowledgements

The authors would like to thank Grand Hotel Huis ter Duin for their cooperation. This research has been supported by the Netherlands Organization for Scientific Research (NWO, grant no. 16352) as part of the Open Technology Programme and by Rijkswaterstaat (Dutch Ministry of Infrastructure and Water Management).

References

Abellán, A., Calvet, J., Vilaplana, J.M., Blanchard, J., 2010. Detection and spatial prediction of rockfalls by means of terrestrial laser scanner monitoring. Geomorphology 119, 162–171.

Anders, K., Lindenbergh, R.C., Vos, S.E., Mara, H., de Vries, S., Höfle, B., 2019. High-frequency 3d geomorphic observation using hourly terrestrial laser scanning data of a sandy beach. ISPRS Annals of Photogrammetry, Remote Sensing and Spatial Information Sciences IV-2-W5, 317–324.

Anders, K., Winiwarter, L., Mara, H., Lindenbergh, R.C., Vos, S.E., Höfle, B., 2021. Influence of spatial and temporal resolution on time series-based coastal surface change analysis using hourly terrestrial laser scans. In: ISPRS Annals of the Photogrammetry, Remote Sensing and Spatial Information Sciences V-2-2021, pp. 137–144. https://doi.org/10.5194/isprs-annals-V-2-2021-137-2021.

Baarda, W., 1968. A Testing Procedure for Use in Geodetic Networks. Publications on Geodesy, New Series 2.

Barbero-García, I., Kuschnerus, M., Vos, S., Lindenbergh, R., 2023. Automatic detection of bulldozer-induced changes on a sandy beach from video using yolo algorithm. Int. J. Appl. Earth Obs. Geoinf. 117, 103185 https://doi.org/10.1016/j.jag.2023.103185.

Bitenc, M., Lindenbergh, R., Khoshelham, K., Van Waarden, A.P., 2011. Evaluation of a LIDAR land-based mobile mapping system for monitoring sandy coasts. Rem. Sens. 3, 1472–1491. https://doi.org/10.3390/rs3071472.

Borradaile, G.J., Borradaile, G., 2003. Statistics of Earth Science Data: Their Distribution in Time, Space, and Orientation, ume 351. Springer.

Brasington, J., Rumsby, B., McVey, R., 2000. Monitoring and modelling morphological change in a braided gravel-bed river using high resolution gps-based survey. Earth Surf. Process. Landforms: the journal of the British Geomorphological Research Group 25, 973–990.

Campos, M.B., Litkey, P., Wang, Y., Chen, Y., Hyyti, H., Hyyppä, J., Puttonen, E., 2021. A long-term terrestrial laser scanning measurement station to continuously monitor structural and phenological dynamics of boreal forest canopy. Front. Plant Sci. 11 https://doi.org/10.3389/fpls.2020.606752 publisher: Frontiers.

Chang, L., Hanssen, R.F., 2016. A probabilistic approach for InSAR time-series postprocessing. IEEE Trans. Geosci. Rem. Sens. 54, 421–430. https://doi.org/10.1109/TGRS.2015.2459037 conference Name: IEEE Transactions on Geoscience and Remote Sensing.

Czerwonka-Schröder, D., 2023. Konzeption einer qualitätsgesicherten Implementierung eines Echtzeitassistenzsystems basierend auf einem terrestrischen Long Range Laserscanner. Ph.D. thesis. Technische Universität Bergakademie Freiberg. URL: https://nbn-resolving.org/urn:nbn:de:bsz:105-qucosa2-857419.

Di Biase, V., Hanssen, R.F., Vos, S.E., 2021. Sensitivity of near-infrared permanent laser scanning intensity for retrieving soil moisture on a coastal beach: calibration procedure using in situ data. Rem. Sens. 13 https://doi.org/10.3390/rs13091645.

Di Biase, V., Kuschnerus, M., Lindenbergh, R.C., 2022. Permanent laser scanner and synthetic aperture radar data: correlation characterisation at a sandy beach. Sensors 22. https://doi.org/10.3390/s22062311.

GeoTilesnl, 2021. Ahn: Actueel Hoogtebestand Nederland. https://GeoTiles.nl.Dataset.

Glennie, C., 2007. Rigorous 3d error analysis of kinematic scanning lidar systems. J. Appl. Geodesy 1, 147–157. https://doi.org/10.1515/jag.2007.017.

Hladik, C., Alber, M., 2012. Accuracy assessment and correction of a lidar-derived salt marsh digital elevation model. Rem. Sens. Environ. 121, 224–235. https://doi.org/10.1016/j.rse.2012.01.018.

Hodgson, M.E., Bresnahan, P., 2004. Accuracy of airborne lidar-derived elevation. Photogramm. Eng. Rem. Sens. 70, 331–339. https://doi.org/10.14358/PERS.70.3.331.

Imparato, D., Teunissen, P., Tiberius, C., 2019. Minimal detectable and identifiable biases for quality control. Surv. Rev. 51, 289–299.

Jin, J., Verbeurgt, J., De Sloover, L., Stal, C., Deruyter, G., Montreuil, A.L., Vos, S., De Maeyer, P., De Wulf, A., 2021. Monitoring spatiotemporal variation in beach surface moisture using a long-range terrestrial laser scanner. ISPRS J. Photogrammetry Remote Sens. 173, 195–208.

Kellerer-Pirklbauer, A., Bauer, A., Proske, H., 2005. Terrestrial laser scanning for glacier monitoring: glaciation changes of the gößnitzkees glacier (schober group, Austria) between 2000 and 2004. In: Proceedings of the 3rd Symposium of the Hohe Tauern National Park for Research in Protected Areas, pp. 97–106. Kaprun, Austria.

Kerekes, G., Schwieger, V., 2020. Elementary error model applied to terrestrial laser scanning measurements: study case arch dam kops. Mathematics 8, 593. https://doi.org/10.3390/math8040593.

Kermarrec, G., Yang, Z., Czerwonka-Schröder, D., 2022. Classification of terrestrial laser scanner point clouds: a comparison of methods for landslide monitoring from mathematical surface approximation. Rem. Sens. 14, 5099.

Koninklijk Nederlands Meteorologisch Instituut. https://www.knmi.nl/nederland-nu/klimatologie/uurgegevens, 2022.

Kuschnerus, M., Lindenbergh, R., Lodder, Q., Brand, E., Vos, S., 2022. Deteching anthropogenic volume changes in cross sections of a sandy beach with permanent laser scanning. Int. Arch. Photogram. Rem. Sens. Spatial Inf. Sci. XLIII-B2–2022, 1055–1061. https://doi.org/10.5194/isprs-archives-XLIII-B2-2022-1055-2022.

Kuschnerus, M., Lindenbergh, R., Vos, S., 2021a. Coastal change patterns from time series clustering of permanent laser scan data. Earth Surf. Dyn. 9, 89–103.

Kuschnerus, M., Schröder, D., Lindenbergh, R., 2021b. Environmental influences on the stability of a permanently installed laser scanner. In: The International Archives of the Photogrammetry, Remote Sensing and Spatial Information Sciences, pp. 745–752. https://doi.org/10.5194/isprs-archives-XLIII-B2-2021-745-2021. Copernicus GmbH.

Lague, D., Brodu, N., Leroux, J., 2013. Accurate 3D comparison of complex topography with terrestrial laser scanner: application to the Rangitikei canyon (N-Z). ISPRS J. Photogrammetry Remote Sens. 82, 10–26. https://doi.org/10.1016/j.isprsjprs.2013.04.009.

Lane, S.N., Westaway, R.M., Murray Hicks, D., 2003. Estimation of erosion and deposition volumes in a large, gravel-bed, braided river using synoptic remote sensing. Earth Surf. Process. Landforms: the journal of the British Geomorphological Research Group 28, 249–271.

Lichti, D.D., 2007. Error modelling, calibration and analysis of an AM–CW terrestrial laser scanner system. ISPRS J. Photogrammetry Remote Sens. 61, 307–324. https://doi.org/10.1016/j.isprsjprs.2006.10.004.

Lindenbergh, R., 2010. Engineering applications. In: Vosselman, G., Maas, H.G. (Eds.), Airborne and Terrestrial Laser Scanning. Whittles Publishing. 7, pp. 237–269.

Marshall, A., 1972. The thermal properties of concrete. Build. Sci. 7, 167–174. https://doi.org/10.1016/0007-3628(72)90022-9.
Medic, T., Holst, C., Kuhlmann, H., 2019. Improving the results of terrestrial laser scanner calibration by an optimized calibration process. In: Proceedings of the Photogrammetrie, Laserscanning, Optische 3D-Messtechnik. Beiträge der Oldenburger 3D-Tage, Oldenburg, Germany, pp. 5–7.
Milan, D.J., Heritage, G.L., Hetherington, D., 2007. Application of a 3D laser scanner in the assessment of erosion and deposition volumes and channel change in a proglacial river. Earth Surf. Process. Landforms 32, 1657–1674. https://doi.org/10.1002/esp.1592.
Mukupa, W., Roberts, G.W., Hancock, C.M., Al-Manasir, K., 2017. A review of the use of terrestrial laser scanning application for change detection and deformation monitoring of structures. Surv. Rev. 49, 99–116. https://doi.org/10.1080/00396265.2015.1133039.
Muralikrishnan, B., 2021. Performance evaluation of terrestrial laser scanners—a review. Meas. Sci. Technol. 32, 072001 https://doi.org/10.1088/1361-6501/abdae3.
Rofatto, V.F., Matsuoka, M.T., Klein, I., Veronez, M.R., Bonimani, M.L., Lehmann, R., 2020. A half-century of baarda's concept of reliability: a review, new perspectives, and applications. Surv. Rev. 52, 261–277. https://doi.org/10.1080/00396265.2018.1548118.
Schmitz, B., Holst, C., Medic, T., Lichti, D.D., Kuhlmann, H., 2019. How to efficiently determine the range precision of 3d terrestrial laser scanners. Sensors 19, 1466.
Schröder, D., Anders, K., Winiwarter, L., Wujanz, D., 2022. Permanent terrestrial lidar monitoring in mining, natural hazard prevention and infrastructure protection–chances, risks, and challenges: a case study of a rockfall in tyrol, Austria. Proceedings of 5th Joint International Symposium on Deformation Monitoring (JISDM).
Schröder, D., Nowacki, A., 2021. Die atmosphäre als restriktiver einfluss auf messergebnisse eines long range laserscanners. Proceedings of 21. Internationale Geodätische Woche 2021.
Soudarissanane, S., 2016. The Geometry of Terrestrial Laser Scanning; Identification of Errors, Modeling and Mitigation of Scanning Geometry. Delft University of Technology, Dissertation.
Soudarissanane, S., Lindenbergh, R., Menenti, M., Teunissen, P., 2011. Scanning geometry: influencing factor on the quality of terrestrial laser scanning points. ISPRS J. Photogrammetry Remote Sens. 66, 389–399. https://doi.org/10.1016/j.isprsjprs.2011.01.005.
Teunissen, P., 2006. Testing Theory. VSSD Delft.
Tiberius, C., van der Marel, H., Reudink, R., van Leijen, F., 2021. Surveying and Mapping. TU Delft Open, Delft, The Netherlands. https://doi.org/10.5074/T.2021.007.
Vezočnik, R., Ambrožič, T., Sterle, O., Bilban, G., Pfeifer, N., Stopar, B., 2009. Use of terrestrial laser scanning Technology for long term high precision deformation monitoring. Sensors 9, 9873–9895. https://doi.org/10.3390/s91209873.
Voordendag, A., Goger, B., Klug, C., Prinz, R., Rutzinger, M., Sauter, T., Kaser, G., 2023. Uncertainty assessment of a permanent long-range terrestrial laser scanning system for the quantification of snow dynamics on hintereisferner (Austria). Front. Earth Sci. 11, 1085416.
Voordendag, A.B., Goger, B., Klug, C., Prinz, R., Rutzinger, M., Kaser, G., 2021. Automated and permanent long-range terrestrial laser scanning in a high mountain environment: setup and first results. ISPRS annals of the photogrammetry. Remote Sensing and Spatial Information Sciences V-2-2021 153–160. https://doi.org/10.5194/isprs-annals-V-2-2021-153-2021.
Vos, S., Anders, K., Kuschnerus, M., Lindenbergh, R., Höfle, B., Aarninkhof, S., de Vries, S., 2022. A high-resolution 4D terrestrial laser scan dataset of the Kijkduin beach-dune system, The Netherlands. Sci. Data 9, 191. https://doi.org/10.1038/s41597-022-01291-9.
Vos, S., Kuschnerus, M., Lindenbergh, R.C., 2020. Assessing the error budget for permanent laser scanning on coastal beaches. Proceedings of FIG Working Week, 2020.
Vos, S., Kuschnerus, M., de Vries, S., Lindenbergh, R., 2023. 4d spatio-temporal laser scan dataset of the beach-dune system in noordwijk, nl. https://data.4tu.nl/datasets/1aac46fb-7900-4d4c-a099-d2ce354811d2/2.
Vos, S., Lindenbergh, R., de Vries, S., 2017. CoastScan: continuous monitoring of coastal change using terrestrial laser scanning. In: Proceedings of Coastal Dynamics 2017. Helsingør, Denmark, pp. 1518–1528.
Wheaton, J.M., Brasington, J., Darby, S.E., Sear, D.A., 2010. Accounting for uncertainty in DEMs from repeat topographic surveys: improved sediment budgets. Earth Surf. Process. Landforms 35, 136–156. https://doi.org/10.1002/esp.1886.
Williams, J.G., Rosser, N.J., Hardy, R.J., Brain, M.J., Afana, A.A., 2018. Optimising 4-D surface change detection: an approach for capturing rockfall magnitude–frequency. Earth Surf. Dyn. 6, 101–119. https://doi.org/10.5194/esurf-6-101-2018 publisher: Copernicus GmbH.
Winiwarter, L., Anders, K., Czerwonka-Schröder, D., Höfle, B., 2023. Full four-dimensional change analysis of topographic point cloud time series using kalman filtering. Earth Surf. Dyn. 11, 593–613.
Winiwarter, L., Anders, K., Höfle, B., 2021. M3C2-EP: pushing the limits of 3D topographic point cloud change detection by error propagation. ISPRS J. Photogrammetry Remote Sens. 178, 240–258. https://doi.org/10.1016/j.isprsjprs.2021.06.011.
Zhou, K., Lindenbergh, R., Gorte, B., 2019. Automatic shadow detection in urban very-high-resolution images using existing 3D models for free training. Rem. Sens. 11, 72. https://doi.org/10.3390/rs11010072 number: 1.
Zoumpekas, T., Puig, A., Salamó, M., García-Sellés, D., Blanco Nuñez, L., Guinau, M., 2021. An intelligent framework for end-to-end rockfall detection. Int. J. Intell. Syst. 36, 6471–6502. https://doi.org/10.1002/int.22557.